https://doi.org/10.5194/egusphere-2026-828
Preprint. Discussion started: 9 March 2026

Inversion of ground ice content using coupled multi-source electromagnetic parameters in the source region of the Yellow River on the Tibetan Plateau

Wei Chen[1,2], Min Xu[2,3*], Weibin Luo[4], Haidong Han[2,3], Wu Wang[2,3], Xi Zhang[2,3], Xingdong Li[1]

[1] *School of Mathematics and Physics, Lanzhou Jiaotong University, Lanzhou 730070, China*

[2] *State Key Laboratory of Cryospheric Science and Frozen Soil Engineering, Northwest Institute of Eco-Environment and Resources, Chinese Academy of Sciences, Lanzhou, 730000, China*

[3] *University of Chinese Academy of Sciences, Beijing, 100049, China*

[4] *Lanzhou Resources & Environment VOC-TECH University, Lanzhou, 730021, China*

** Corresponding author. E-mail addresses: xumin@lzb.ac.cn (Min Xu).*

https://doi.org/10.5194/egusphere-2026-828
Preprint. Discussion started: 9 March 2026

ABSTRACT

Ground ice content plays a key role in controlling permafrost stability in the source region of the Yellow River, yet its quantitative characterization is limited by strong subsurface heterogeneity and scarce direct observations. This study integrated ground-penetrating radar (GPR) and opposing coils transient electromagnetic (OCTEM) data within a joint inversion framework based on full-waveform inversion (FWI) to estimate volumetric ice content (VIC) at four high-altitude permafrost sites. The results showed strong lateral and vertical variability in VIC, with distinct VIC magnitudes and depth-dependent patterns among sites. Shallow VIC derived from radar-based dielectric properties provided physical constraints for estimating deeper VIC through a calibrated relationship between relative permittivity and apparent resistivity. Ice-rich and ice-poor zones were spatially consistent with apparent resistivity sections and forward-modeled electromagnetic responses, supporting the reliability of the integrated approach. Estimated VIC at depths from 2 to 10 m was relatively low at Huashixia, at approximately 8-15%, but generally exceeded 20% at Hela, Shuangchagou, and Maduo. This study demonstrated the effectiveness of a physically constrained electromagnetic strategy for quantifying VIC in alpine permafrost.

Keywords: GPR; OCTEM; permafrost; volumetric ice content; joint inversion

1. Introduction

Permafrost regions are fundamental components of cold-region environments, exerting strong control over hydrology, soil stability, and ecosystem functioning (Yang et al., 2024). Ground ice, a major constituent of permafrost, is widespread in high-altitude areas such as the Qinghai-Tibet Plateau (QTP), influencing active layer dynamics, ground deformation, and the thermal and mechanical properties of frozen soils (Wang et al., 2018; Lin et al., 2020). Variations in volumetric ice content (VIC) affect thaw settlement, infrastructure stability, groundwater storage, and surface-groundwater interactions (Aga et al., 2023). Under ongoing climate warming, permafrost degradation and ground ice thaw have led to a deepening active layer, thaw-induced

https://doi.org/10.5194/egusphere-2026-828
Preprint. Discussion started: 9 March 2026

subsidence, and altered subsurface hydrology, with cascading effects on slope stability, hydrological connectivity, and ecosystem services (Yuan et al., 2020; Jin et al., 2022). Quantitative estimation of VIC is therefore critical for understanding permafrost dynamics and assessing environmental changes in high-altitude regions.

Quantitative estimation of VIC remains challenging due to the pronounced heterogeneity of permafrost and the scarcity of direct measurements, particularly in high-altitude and remote regions (Faucher et al., 2024). Borehole drilling and in situ sampling provide reliable point-scale information, but are labor-intensive, costly, and spatially sparse, which severely limits their applicability over extensive permafrost areas (Hilbich et al., 2022a; Roustaei et al., 2025). In regions such as the source area of the Yellow River, complex terrain, harsh climatic conditions, and logistical constraints further hinder large-scale field investigations, resulting in a critical lack of subsurface ground-truth data (Wang et al., 2018; Jin et al., 2022; Yang et al., 2023). Consequently, many previous studies have inferred VIC indirectly by combining limited borehole data with geomorphological interpretation, ground temperature observations, empirical relationships, or machine learning approaches (Wang et al., 2018; Zou et al., 2024). Although these methods have improved understanding of permafrost conditions, the resulting estimates often involve substantial uncertainties arising from parameter non-uniqueness, scale mismatches, and the complex coupling between thermal, hydrological, and mechanical processes (García-Pereira et al., 2025). As a result, reliable regional-scale characterization of VIC in data-scarce permafrost regions remains limited.

Electromagnetic geophysical methods, including ground-penetrating radar (GPR) and transient electromagnetic (TEM) surveys, offer non-invasive and efficient means to investigate frozen ground (Briggs et al., 2017). These methods are sensitive to contrasts in relative permittivity and apparent resistivity, which are physically linked to variations in unfrozen water and VIC (Anbazhagan et al., 2020). Exploiting these contrasts, electromagnetic surveys can delineate frozen layers, ice-rich zones, and subsurface structures, providing spatially continuous information unattainable from boreholes alone (Ekimova et al., 2026). Recent studies have demonstrated the potential of electromagnetic methods for mapping permafrost and identifying ground ice, yet most applications remain qualitative or semi-quantitative, or rely on auxiliary borehole data for calibration (Ge et al., 2025). Quantitative inversion of VIC is further

https://doi.org/10.5194/egusphere-2026-828
Preprint. Discussion started: 9 March 2026

complicated by trade-offs among electromagnetic parameters and the limited use of physically constrained multi-parameter integration (Mollaret et al., 2020). Robust frameworks that quantitatively estimate VIC using electromagnetic observations alone therefore remain scarce, particularly in remote permafrost regions with sparse direct measurements.

This study focused on the source region of the Yellow River and aimed to advance quantitative estimation of VIC using multi-source electromagnetic data. By exploiting the complementary sensitivities of relative permittivity and apparent resistivity, and by enforcing their physically consistent relationship with VIC, a physically constrained electromagnetic framework was developed to quantify VIC across heterogeneous permafrost terrains without reliance on extensive borehole measurements. Quantitative estimation in this study refers to the physically constrained inversion of VIC from electromagnetic parameters, rather than empirical classification or relative assessment. By jointly constraining relative permittivity and apparent resistivity information within a unified framework, the proposed approach reduced parameter non-uniqueness and improved the robustness of VIC estimation in complex permafrost settings. This framework facilitates improved interpretation of permafrost structure, subsurface hydrology, and freeze-thaw processes, providing insights relevant for geotechnical planning, hydrological modeling, and climate impact assessment in alpine cold environments. The methodology is transferable to other high-altitude permafrost regions where direct measurements are sparse or logistically challenging, offering a scalable strategy for monitoring and characterizing VIC.

2. Study Area

The source region of the Yellow River, located in the northeastern QTP, constitutes one of the largest continuous permafrost regions in China and represents a typical high-altitude permafrost environment characterized by complex terrain, a cold-arid climate, and widespread ground ice (Yang et al., 2023). The study area extends approximately from 95°50′ to 98°55′ E and from 33°32′ to 35°35′ N, encompassing a total area of about 28,311 km². Permafrost underlies approximately 24,065 km² of this region, accounting for nearly 85.1% of the total area, whereas the remaining portions are predominantly characterized by seasonally frozen ground (Wang et al.,

https://doi.org/10.5194/egusphere-2026-828
Preprint. Discussion started: 9 March 2026

2018). The mean annual ground temperature across the permafrost zone is generally below 0°C (Fig. 1). Regional elevations mostly exceed 4,200 m a.s.l., and the terrain is characterized by extensive plateau surfaces, gently undulating hills, and wide, shallow valleys. Despite the relatively low surface relief, subsurface structures exhibit pronounced heterogeneity (Jin et al., 2022). Under sustained low-temperature conditions and intensive freeze-thaw processes, ground ice is widely developed, and its spatial distribution and volumetric content are jointly controlled by topography, soil texture, and hydrothermal regimes. Within the permafrost zone, VIC generally ranges from 20 to 40% at depths of 2-10 m (Zou et al., 2024). In this study, four representative sites, Huashixia, Hela, Shuangchagou, and Maduo, were selected to quantify VIC using a multi-source electromagnetic-based approach. These sites were chosen to cover the main geographic distribution of the Yellow River source region and to facilitate field measurements in accessible locations.

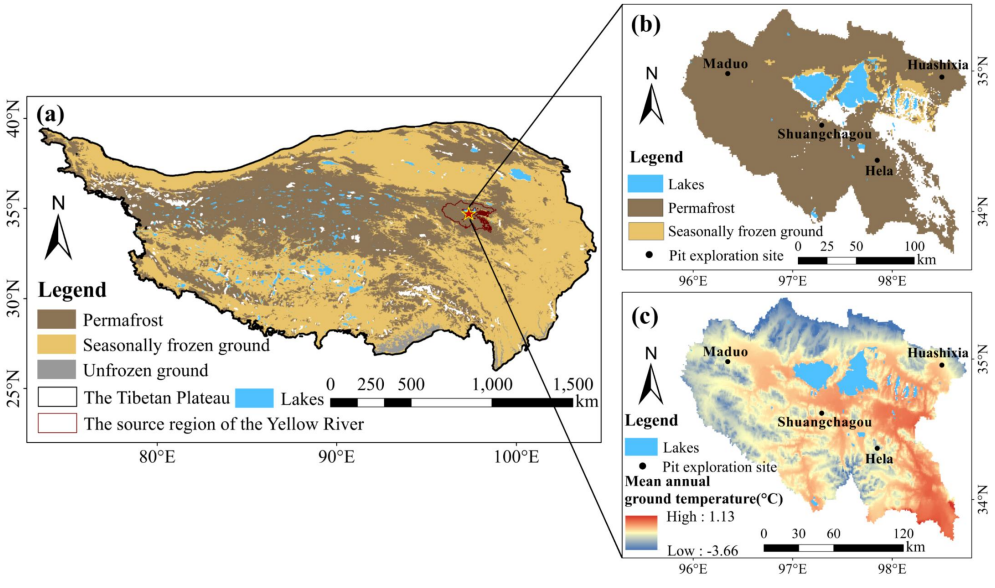

Fig. 1. Study area.

3. Data and Methods

3.1 Data

https://doi.org/10.5194/egusphere-2026-828
Preprint. Discussion started: 9 March 2026

Accurate characterization of VIC in the Yellow River source region requires comprehensive field observations due to complex permafrost conditions, high elevations, and pronounced subsurface heterogeneity. Field datasets were collected at four representative sites: Huashixia, Hela, Shuangchagou, and Maduo (Fig. 2). In November 2024, dual-frequency GPR surveys using a Jietan system at 100 and 400 MHz captured subsurface reflection patterns from minimally processed profiles (Fig. 3). Complementary opposing coils transient electromagnetic (OCTEM) measurements acquired using an HPTEM-18 system were used to map spatial variations in subsurface resistivity (Fig. 4). Shallow soil pits were excavated for sample collection with a ring knife, and laboratory analyses determined total volumetric water content (TVWC) across shallow depth intervals. Ground temperature data for 2013 to 2015 were obtained from the National Tibetan Plateau Data Center (TPDC) with a temporal resolution of 1 to 10 years and spatial resolution from 100 m to 1 km (Li et al., 2016). Combined, these multi-source datasets provided a physically constrained basis for quantitative inversion, enabling robust estimation of ground-ice content without extensive borehole measurements.

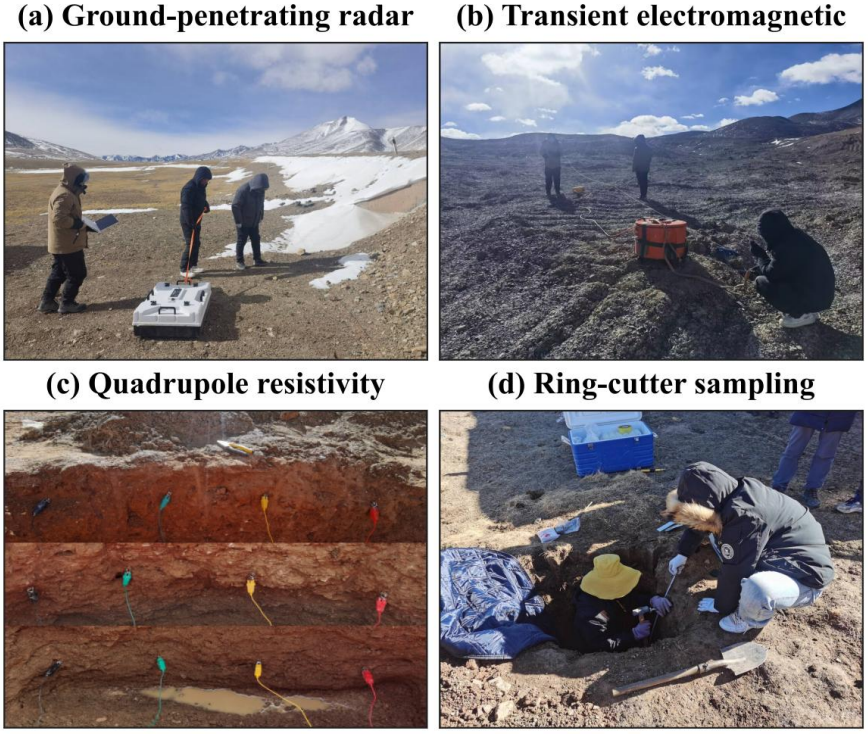

Fig. 2. Field data collection.

https://doi.org/10.5194/egusphere-2026-828
Preprint. Discussion started: 9 March 2026

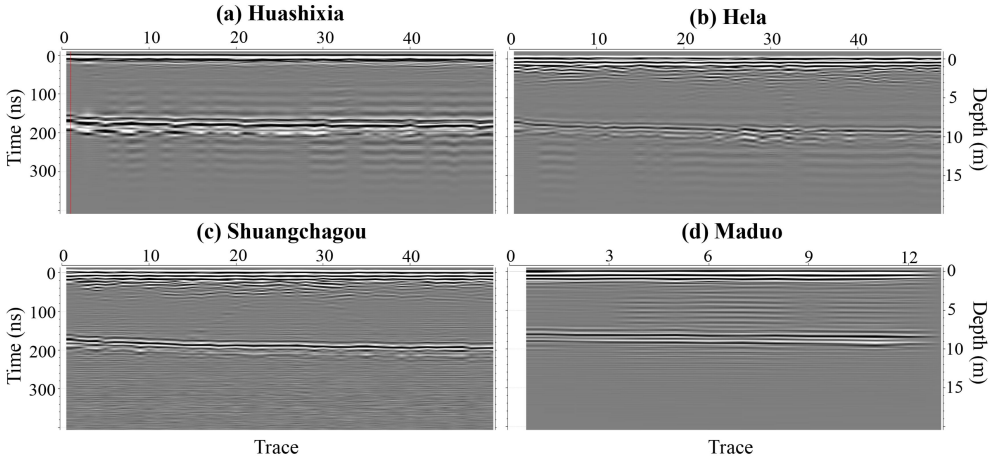

Fig. 3. Dual-frequency GPR profiles with minimal processing.

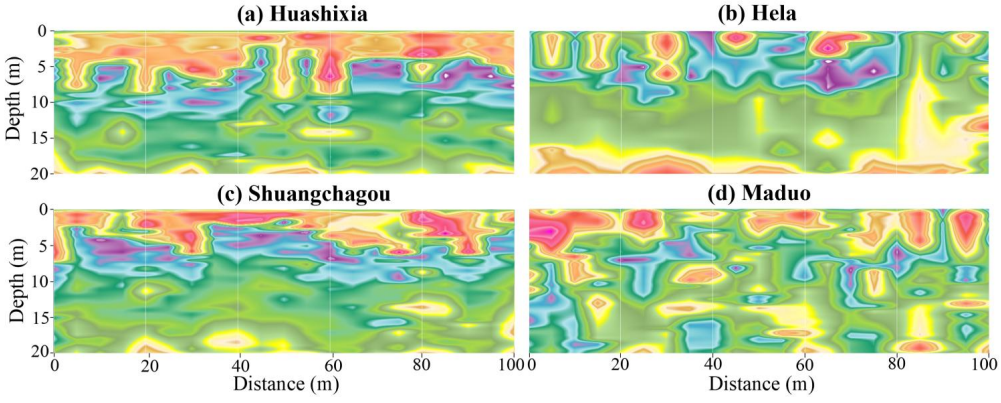

Fig. 4. OCTEM-derived subsurface resistivity profiles.

3.2 Methods

3.2.1 Finite-Difference Time-Domain (FDTD)

In this study, electromagnetic wave propagation was simulated using the finite-difference time-domain (FDTD) approach, which served as the numerical foundation for both forward modeling and full-waveform inversion (FWI). Rather than relying on frequency-domain formulations, the FDTD approach solves Maxwell's equations directly in the time domain, making it particularly suitable for modeling wave propagation and scattering in subsurface

https://doi.org/10.5194/egusphere-2026-828
Preprint. Discussion started: 9 March 2026

environments characterized by strong material contrasts and geometric complexity. Owing to its explicit formulation and flexibility, this method has been extensively adopted in geophysical electromagnetic simulations involving heterogeneous media. Within the FDTD framework, the computational domain is discretized following the Yee lattice arrangement, where electric and magnetic field components are positioned at staggered locations inside each grid cell. This spatial staggering allows the curl relationships between electric and magnetic fields to be naturally satisfied in the discrete formulation. Temporal and spatial derivatives are approximated using second-order central difference operators, converting the continuous Maxwell equations into a set of explicit time-stepping equations that can be advanced sequentially. To ensure numerical stability during time integration, the simulation time step is restricted according to the Courant–Friedrichs–Lewy (CFL) stability criterion. During the marching process, electric and magnetic field components are updated alternately in a leap-frog scheme, enabling realistic simulation of wave propagation, reflection, and energy attenuation within heterogeneous frozen ground. To suppress non-physical reflections from model boundaries, perfectly matched layer (PML) absorbing boundaries are applied around the computational domain, effectively minimizing artificial boundary effects (Teixeira et al., 2023).

The governing equations for the FDTD formulation are briefly summarized below (adapted from Garcıa et al., n.d.). Electromagnetic wave propagation in the subsurface is described by Maxwell's equations, which in the time domain can be written in curl form as (L. Liu et al., 2025):

$$\nabla \times E = -\mu \frac{\partial H}{\partial t} \tag{1}$$

$$\nabla \times H = \varepsilon \frac{\partial E}{\partial t} + J \tag{2}$$

where E and H denote the electric and magnetic field vectors (V/m and A/m), respectively; ε is the absolute permittivity (F/m), μ is the magnetic permeability (H/m), σ represents the electrical conductivity (S/m), J is the electric current density (A/m^2), and t denotes time (s). By discretizing the curl equations on the Yee grid and applying second-order finite differences in both space and time, the electric field components can be updated explicitly. For example, the x-component of the electric field is given by:

https://doi.org/10.5194/egusphere-2026-828
Preprint. Discussion started: 9 March 2026

$$E_x^{n+1}(i,j,k) = E_x^n(i,j,k) + \frac{\Delta t}{\varepsilon}\left[\frac{H_x^{n+\frac{1}{2}}(i,j,k) - H_x^{n+\frac{1}{2}}(i,j-1,k)}{\Delta y} - \frac{H_y^{n+\frac{1}{2}}(i,j,k) - H_y^{n+\frac{1}{2}}(i,j,k-1)}{\Delta z}\right] \quad (3)$$

where i, j, and k indicate spatial indices along the x-, y-, and z-directions, respectively; n denotes the discrete time level; Δt is the temporal increment (s); and Δy and Δz are the spatial grid spacings (m). Magnetic field components are updated in a similar fashion but are offset by half a time step relative to the electric field, forming a staggered leap-frog integration scheme. For instance, the x-component of the magnetic field is given by:

$$H_x^{n+\frac{1}{2}}(i,j,k) = H_x^{n-\frac{1}{2}}(i,j,k) - \frac{\Delta t}{\mu}\left[\frac{E_z^n(i,j+1,k) - E_z^n(i,j,k)}{\Delta y} - \frac{E_y^n(i,j,k+1) - E_y^n(i,j,k)}{\Delta z}\right] \quad (4)$$

To guarantee numerical stability of the explicit time-marching scheme, the time step must satisfy the CFL criterion. In three-dimensional space, this condition can be written as:

$$\Delta t \le 1/c\sqrt{1/\Delta x^2 + 1/\Delta y^2 + 1/\Delta z^2} \quad (5)$$

where c denotes the electromagnetic wave propagation velocity in the medium (m/s), and Δx, Δy, and Δz are the grid spacings along the three coordinate directions (m).

3.2.2 Ground-Penetrating Radar (GPR)

GPR is an active electromagnetic sensing technique that images subsurface structures by transmitting short-duration, high-frequency electromagnetic pulses into the ground and recording the reflected signals generated at interfaces with contrasting electromagnetic properties. Reflections occur primarily due to spatial variations in relative permittivity and electrical conductivity, which control wave velocity, attenuation, and reflection strength. In a typical GPR survey, an emitting antenna radiates electromagnetic pulses into the subsurface, while a receiving antenna records the backscattered wavefield as a function of two-way travel time. The recorded signals contain information on the geometry, depth, and electromagnetic characteristics of subsurface targets. Because radar-wave velocity is mainly governed by relative permittivity, variations in recorded travel times and amplitudes can be used to infer changes in material composition, moisture state, and VIC. Owing to its high spatial resolution, rapid data acquisition,

https://doi.org/10.5194/egusphere-2026-828
Preprint. Discussion started: 9 March 2026

and non-invasive nature, GPR has been widely applied in geological investigations, engineering surveys, underground utility detection, and archaeological studies (Zhang et al., 2022). The common-offset reflection profiling configuration represents the most fundamental and widely used acquisition mode in GPR surveys. In this configuration, the transmitting and receiving antennas are maintained at a fixed separation and moved simultaneously along the same survey line. Reflection signals are continuously recorded as the antenna pair advances at a constant speed, producing a two-dimensional subsurface reflection image, commonly referred to as a B-scan (Fig. 5). This acquisition mode offers operational simplicity, high efficiency, and intuitive imaging, making it suitable for a broad range of near-surface investigations.

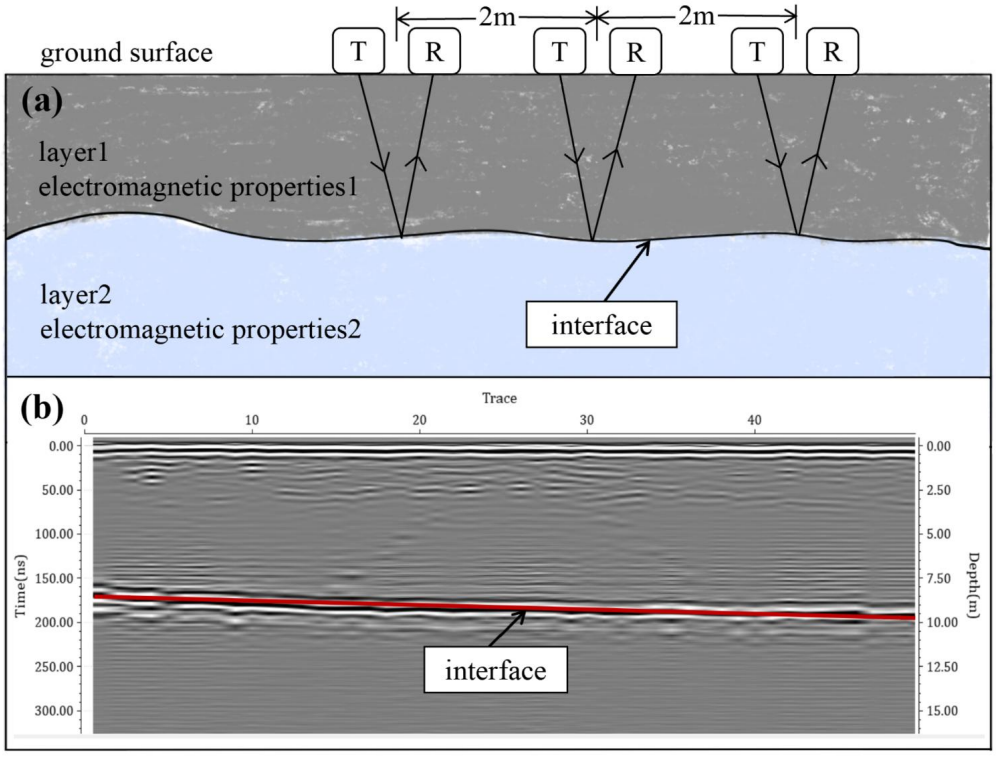

Fig. 5. (a) Schematic illustration of the GPR survey configuration (T is the transmitting antenna, and R is the receiving antenna); (b) real GPR profile data.

In this study, GPR data were acquired using a Jietan dual-frequency system in a common-offset reflection profiling configuration. The survey line length was 100 m, with a trace spacing of 2 m and 32-fold stacking to enhance signal quality. The relative permittivity was set to

https://doi.org/10.5194/egusphere-2026-828
Preprint. Discussion started: 9 March 2026

9 during data acquisition, with 1,024 sampling points and a sampling rate of 1 GHz. Raw GPR data were processed using a standard workflow that included time-zero correction, dewow filtering, band-pass filtering, and gain correction. These procedures were applied to suppress low-frequency noise, enhance reflection continuity, and improve the signal-to-noise ratio. The processed GPR profiles provided the primary observational constraints for subsequent forward modeling and FWI.

3.2.3 Opposing Coils Transient Electromagnetic (OCTEM)

OCTEM is an advanced time-domain electromagnetic technique for high-precision imaging of deeper subsurface structures, with a detection depth of up to approximately 100 m. It is highly sensitive to variations in subsurface conductivity, making it particularly suitable for high-resolution investigations. The core principle of OCTEM relies on a dual-transmitter coil configuration, in which two coaxial, parallel, and identical coils are energized with synchronous currents of equal magnitude but opposite directions, forming a zero-flux plane at the midpoint between the coils. The receiving coil is positioned on this zero-flux plane to suppress the primary field and record only the secondary field induced by subsurface eddy currents after the transmitter current is abruptly turned off (Fig. 6). Based on electromagnetic induction and Maxwell's equations, the decay characteristics of the secondary field are used to invert the apparent resistivity distribution, thereby reconstructing the electrical structure of subsurface media. Compared with traditional TEM methods, OCTEM effectively mitigates early-signal distortion and the shallow detection blind zone caused by the self-inductance of the receiving coil during primary field turn-off. Its advantages include high signal-to-noise ratio, superior lateral resolution, and energy concentration, making it widely applicable to engineering geology, environmental studies, urban underground space investigations, and shallow mineral resource exploration.

https://doi.org/10.5194/egusphere-2026-828
Preprint. Discussion started: 9 March 2026

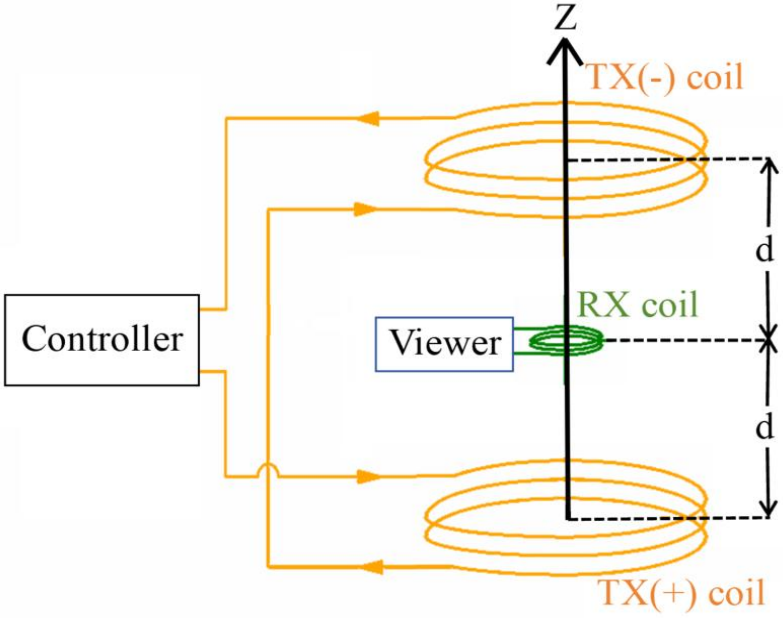

Fig. 6. Schematic illustration of the OCTEM survey configuration (Wei et al., 2023).

In this study, OCTEM measurements were carried out using an HPTEM-18 system. The survey line locations and lengths were identical to those of the GPR measurements, with a station spacing of 5 m. Apparent resistivity was calculated from the acquired OCTEM responses according to the following relationship (Yang et al., 2022):

$$\rho_a = \left(\frac{I \cdot AR \cdot AT}{V}\right)^{2/3} \cdot \left(\frac{1}{t}\right)^{5/3} \cdot 6.3219E-3 \quad (6)$$

where I is the transmitted current (A), A_R and A_T are the areas of the receiving and transmitting coils (m²), and t is the time (μs). This methodology provided a reliable quantitative basis for characterizing subsurface apparent resistivity, which is critical for constraining VIC inversion in the study area.

3.2.4 gprMax Forward Modeling

gprMax is a forward modeling software for GPR using FDTD and Yee's staggered grid. It discretizes Maxwell's equations in space and time to simulate electromagnetic wave propagation by updating electric and magnetic fields. PML boundaries suppress nonphysical reflections and

https://doi.org/10.5194/egusphere-2026-828
Preprint. Discussion started: 9 March 2026

allow simulation of anisotropic and dispersive media (e.g., Debye) and rough surfaces. Users can choose 2D TMz or 3D wave modes, set antenna configurations, transmitted waveforms, and medium properties like relative permittivity and conductivity. The software outputs time-domain echoes (A-scan) and reflection profiles (B-scan/C-scan) showing subsurface responses. OpenMP parallelization and CUDA GPU acceleration speed up simulations of reflection, refraction, and attenuation caused by dielectric contrasts between ground ice and permafrost.These features support inversion and imaging optimization, as well as analysis of VIC distribution (Warren et al., 2016).

In this study, apparent resistivity data acquired from OCTEM measurements were used to classify subsurface media, thereby defining key physical parameters, including relative permittivity and electrical conductivity, for each medium. To ensure consistency between numerical simulation and field observations, system parameters, such as the GPR antenna configuration and transmitted waveforms, were fully aligned with the specifications of the field-deployed GPR system. Considering the computational complexity and limited practical benefit of explicitly simulating dual-frequency antennas, the forward modeling was conducted using a single central frequency of 100 MHz. This frequency was selected because it provided sufficient penetration depth to match the target investigation depth of 20 m, while maintaining stable numerical performance and reliable representation of subsurface electromagnetic responses.

3.2.5 Full-Waveform Inversion (FWI)

FWI was implemented within FDTD framework to estimate the subsurface relative permittivity distribution. The inversion follows an iterative optimization procedure, including forward simulation of electromagnetic wavefields, misfit evaluation between simulated and observed GPR data, and gradient-based updating of model parameters. The forward problem is solved using an FDTD solver on a structured grid, where electromagnetic wave propagation is computed for a given relative permittivity model. The simulated radar responses are compared with the observed data to construct an objective function, defined as the mean squared error between simulated and observed waveforms. To enhance numerical stability and suppress

https://doi.org/10.5194/egusphere-2026-828
Preprint. Discussion started: 9 March 2026

nonphysical oscillations, a regularization term enforcing spatial smoothness of the relative permittivity field is incorporated. The objective function Φ(m) is expressed as:

$$\Phi(m) = \frac{1}{2}\sum_{s,r}\int_0^T \left[d_{cal}(s,r,t;m) - d_{obs}(s,r,t)\right]^2 dt + \lambda R(m) \tag{7}$$

where d_{obs} is the observed GPR waveform and d_{cal} is the simulated GPR waveform; m is the relative permittivity model; s and r are the source-receiver pairs; $R(m)$ is a smoothness-based regularization term; and λ is the regularization weight. The relative permittivity is treated as the primary inversion parameter and is optimized using a gradient-based algorithm implemented in the PyTorch framework, enabling automatic differentiation of the objective function with respect to model parameters. Parameter updates are performed using the Adam optimizer, and gradient clipping is applied to prevent numerical instability during backpropagation (L. Liu et al., 2025). The gradient of the objective function with respect to the model parameters and the parameter update are calculated as follows:

$$\nabla_{\varepsilon_r}\Phi = \frac{\partial \Phi}{\partial \varepsilon_r} \tag{8}$$

$$\varepsilon_r^{k+1} = \varepsilon_r^k - \alpha_k \nabla_{\varepsilon_r}\Phi \tag{9}$$

where k denotes the iteration index and α_k is the adaptive step size determined by the Adam optimizer.

The initial relative permittivity model was derived from forward modeling based on prior geological interpretation and assigned electromagnetic properties, providing a physically consistent starting point and ensuring compatibility between forward and inverse simulations. To improve computational efficiency and robustness, several strategies were employed, including adaptive handling of source-receiver geometry, parameter constraints for electromagnetic properties, and PML absorbing boundary conditions. The inversion terminated based on predefined stopping criteria considering iteration count and misfit evolution. Overall, the proposed FWI workflow established a consistent, reproducible, and physically constrained framework for integrating electromagnetic forward modeling and inversion in subsurface relative permittivity characterization.

https://doi.org/10.5194/egusphere-2026-828
Preprint. Discussion started: 9 March 2026

3.2.6 Shallow VIC Inversion Algorithm

A systematic workflow was developed to quantify shallow VIC by integrating laboratory-based soil measurements with relative permittivity derived from FWI. The workflow consists of three sequential steps: (1) determination of TVWC (θ_v^{total}, %) from soil samples, (2) estimation of volumetric liquid water content (VLWC, θ_w, %) using FWI-derived relative permittivity, and (3) calculation of VIC by difference.

Soil samples were collected using a standard ring knife, and the TVWC of each depth layer was determined using the gravimetric method. This gravimetric method follows the ASTM D2216 standard for soil moisture determination (D18 Committee, n.d.). The corresponding calculation formulas are as follows:

$$\theta_m = \frac{m_1 - m_2}{m_2} \times 100\% \tag{10}$$

$$\rho_b = \frac{m_2}{V} \tag{11}$$

$$\theta_v^{total} = \theta_m \times \rho_b \tag{12}$$

The key parameters are defined in Table 1.

Table 1 Definition of parameters.

Symbol	Unit	Definition
m_1	g	Mass of wet soil in the ring knife: total mass of ring knife plus field-moist soil minus ring knife mass
m_2	g	Mass of dry soil after oven-drying at 105°C to constant weight
V	cm^3	Ring knife volume (121.11 cm^3 in this study)
θ_m	%	Gravimetric water content: water mass per unit mass of dry soil
ρ_b	g/cm^3	Bulk density: dry soil mass per unit soil volume
θ_v	%	Volumetric water content: water volume per unit soil volume

The VLWC was estimated from the FWI-derived relative permittivity (ε_r) using empirical dielectric to volumetric water content (VWC) relationships reported in previous laboratory studies. Three widely used empirical models were applied:

$$\theta_w^{Topp} = -0.053 + 0.0292\varepsilon_r - 0.00055\varepsilon_r^2 + 0.0000043\varepsilon_r^3 \tag{13}$$

https://doi.org/10.5194/egusphere-2026-828
Preprint. Discussion started: 9 March 2026

$$\theta_w^{Ledieu} = -0.1758 + 0.1138\sqrt{\varepsilon_r} \quad (14)$$

$$\theta_w^{Roth} = -0.0728 + 0.0448\varepsilon_r - 0.00195\varepsilon_r^2 + 0.0000361\varepsilon_r^3 \quad (15)$$

To reduce model-dependent uncertainty, the liquid water content of each layer was calculated as the arithmetic mean of the three estimates:

$$\theta_w^{layer} = \frac{\theta_w^{Topp} + \theta_w^{Ledieu} + \theta_w^{Roth}}{3} \quad (16)$$

Finally, the VIC (θ_i, %) was obtained by subtracting the VLWC from the TVWC:

$$\theta_i = \theta_v^{total} - \theta_w^{layer} \quad (17)$$

This integrated workflow provided a consistent and reproducible approach for converting laboratory soil measurements and FWI-derived dielectric properties into quantitative estimates of shallow VIC, thereby enabling further analysis of permafrost characteristics.

3.2.7 Error Evaluation Metrics

To quantitatively evaluate the accuracy of the inversion results, two widely used error metrics, the root-mean-square error (RMSE) and the mean absolute error (MAE), were employed to quantify discrepancies between predicted values and reference measurements and to provide complementary measures of model performance (Hodson, 2022). The RMSE characterizes the overall deviation between predicted and reference values, with larger errors receiving greater weight. It is defined as:

$$RMSE = \sqrt{\frac{1}{N}\sum_{i=1}^{N}\left(x_i^{pred} - x_i^{ref}\right)^2} \quad (18)$$

where x_i^{pred} is the predicted value of the parameter for the i-th data point (%), x_i^{ref} is the corresponding reference value (%), N is the total number of data points.The MAE measures the average magnitude of absolute deviations between predicted and reference values and is expressed as:

$$MAE = \frac{1}{N}\sum_{i=1}^{N}\left|x_i^{pred} - x_i^{ref}\right| \quad (19)$$

where all symbols and units are consistent with those defined for the RMSE. By jointly

https://doi.org/10.5194/egusphere-2026-828
Preprint. Discussion started: 9 March 2026

applying RMSE and MAE, the inversion accuracy was robustly evaluated, capturing both the sensitivity to large deviations and the typical magnitude of prediction errors. This unified evaluation framework ensured consistent quantitative assessment of VIC estimation.

4. Results

4.1 Permafrost Structure and Electromagnetic Parameter Characteristics

The OCTEM-derived apparent resistivity pseudosections revealed pronounced spatial heterogeneity in the shallow subsurface and clear contrasts in apparent resistivity magnitude among the four investigated sites (Fig. 7). Overall, Huashixia was characterized by relatively low to moderate apparent resistivity values, whereas Hela, Shuangchagou, and Maduo exhibited generally higher apparent resistivity ranges, with maximum values reaching several thousand ohm·m. At most survey locations, apparent resistivity showed a general increasing trend with depth. In contrast, the shallow subsurface displayed pronounced high apparent resistivity anomalies and strong lateral variability, while apparent resistivity patterns gradually became more laterally continuous and uniform at greater depths. These features provided essential constraints on frozen ground structure and electromagnetic parameter distribution, forming the basis for subsequent forward modeling and inversion analyses.

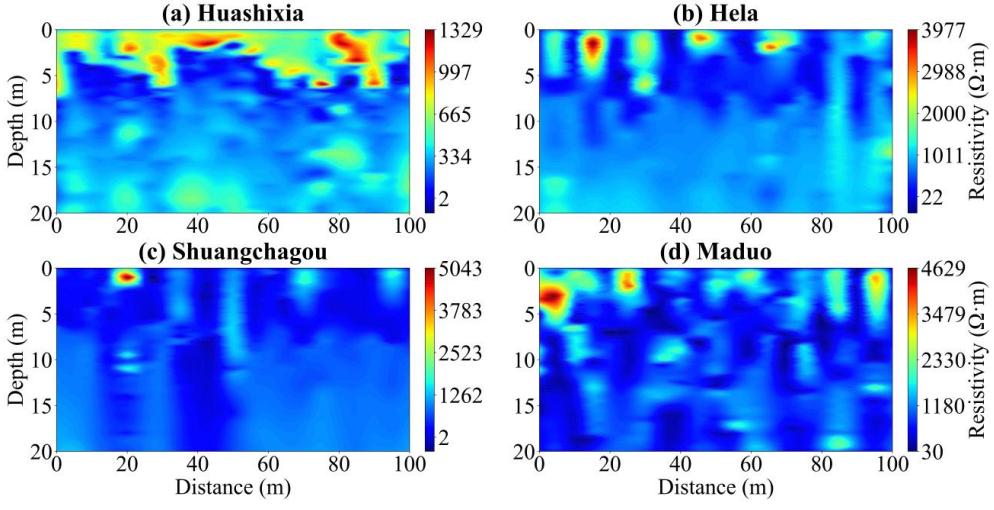

Fig. 7. Apparent resistivity pseudosections.

https://doi.org/10.5194/egusphere-2026-828
Preprint. Discussion started: 9 March 2026

Based on the apparent resistivity characteristics and field observations, forward models for the four study sites were constructed to represent site-specific frozen ground structures and contrasts in electromagnetic properties (Fig. 8). Relative permittivity values were assigned according to the general relationship among apparent resistivity, VWC, and VIC, whereby higher apparent resistivity was commonly associated with higher VIC and lower relative permittivity. Notably, Huashixia exhibited relatively lower apparent resistivity compared with the other sites, which may be attributed not solely to higher VLWC but also to enhanced surface conduction associated with fine-grained materials, bound water films, and elevated pore-water salinity. Under such conditions, electrical conductivity could be significantly increased, whereas the radar-frequency dielectric response remained dominated by ice, soil matrix, and bound water, which exhibited comparatively low polarizability. Consequently, relatively lower relative permittivity values were assigned to Huashixia in the forward model to represent moist but ice-bearing mixed frozen materials and to maintain consistency with the FWI-derived dielectric response and observed GPR wave propagation characteristics.

Across all four sites, the upper several meters exhibited pronounced heterogeneity in material composition, whereas deeper sections gradually transitioned into comparatively more uniform frozen layers with locally developed ice-rich units. At Huashixia, the shallow subsurface was dominated by seasonally frozen and mixed frozen soils, with laterally discontinuous ice-rich frozen soil and sporadic ice lenses embedded within a heterogeneous matrix, reflecting moderate ice accumulation. Hela displayed clearer vertical differentiation, characterized by a shallow active layer and weakly frozen soils overlying laterally continuous ice-rich strata, with occasional gravel or bedrock exposures, indicating relatively stable permafrost conditions. In Shuangchagou, localized anomalies were evident, where wet or weakly frozen materials coexist with high apparent resistivity ice-rich layers and discrete ice lenses within an otherwise frozen background. Maduo was characterized by extensive ice-rich frozen soil and thick ice-bearing layers, with ice lenses and dense bedrock interspersed in intermediate depths, indicating high VIC and a structurally complex frozen ground system. Overall, the forward models effectively captured the primary contrasts in frozen ground architecture and electromagnetic parameterization among the four sites, providing a physically consistent framework for subsequent FWI and quantitative estimation of VIC.

https://doi.org/10.5194/egusphere-2026-828
Preprint. Discussion started: 9 March 2026

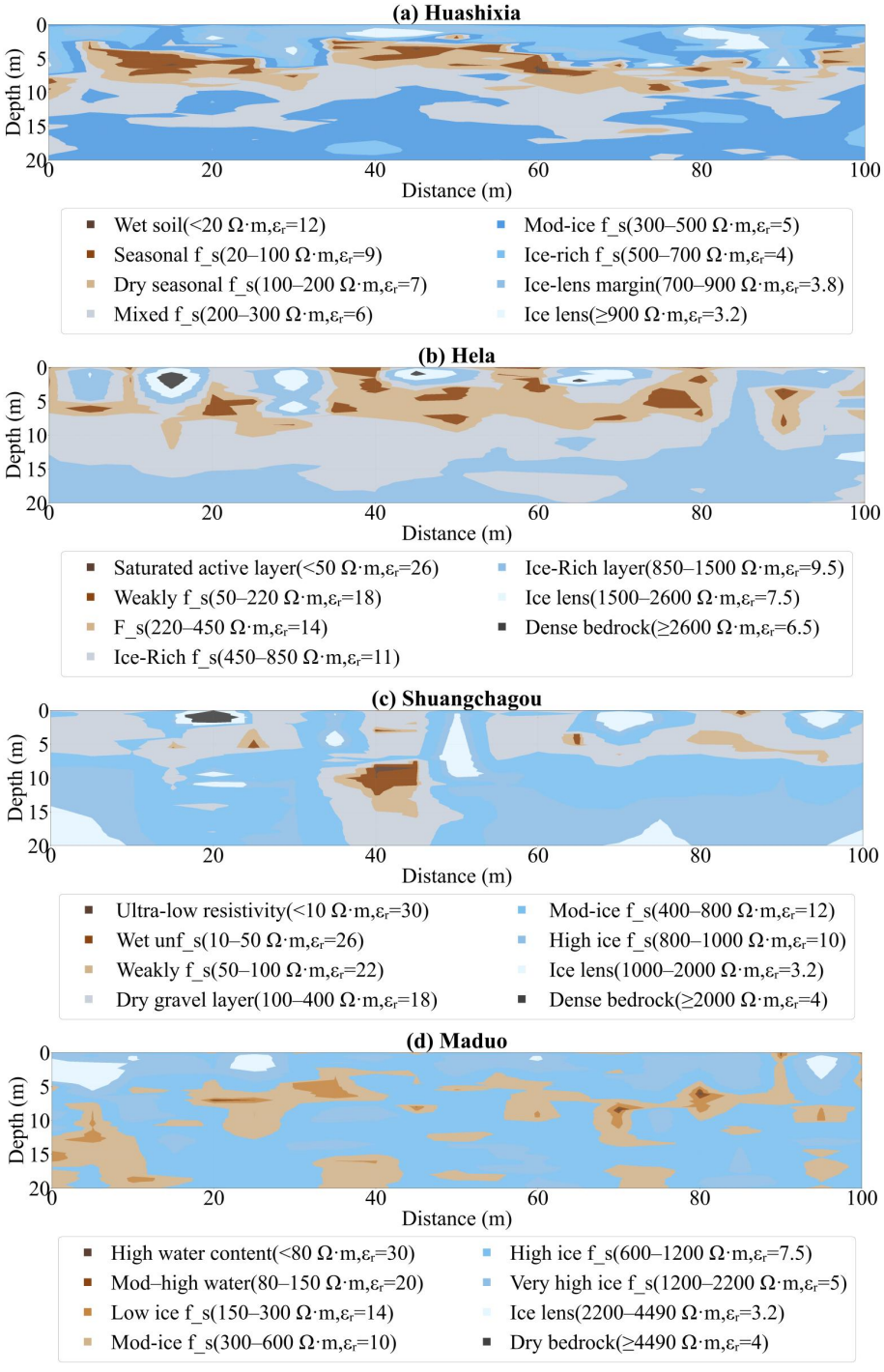

Fig. 8. gprMax forward models (f_s denotes frozen soil).

https://doi.org/10.5194/egusphere-2026-828
Preprint. Discussion started: 9 March 2026

FWI yielded refined subsurface relative permittivity distributions that closely followed the structural patterns of the initial forward models, with only minor perturbations reflecting physically plausible adjustments (Fig. 9). Across all study sites, the shallow subsurface exhibited strong lateral and vertical heterogeneity, characterized by alternating high- and low-permittivity zones over short spatial scales, corresponding to seasonally frozen and mixed frozen soils interspersed with sporadic ice lenses. In contrast, deeper layers generally displayed more uniform relative permittivity distributions, punctuated by discrete high relative permittivity features associated with locally developed ice-rich units. The maximum, mean, and root-mean-square differences between the initial and inverted models were all constrained within approximately 0.05, indicating that the inversion preserved the overall structural integrity without introducing spurious artifacts. Collectively, the FWI results provided a spatially continuous and high-fidelity representation of relative permittivity, forming a robust basis for subsequent quantitative estimation of VIC.

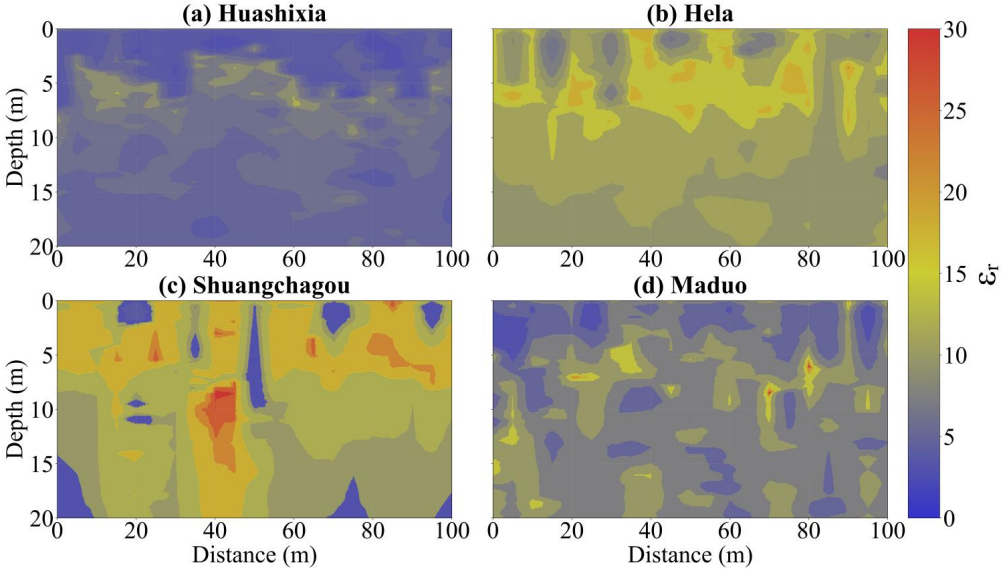

Fig. 9. FWI-derived relative permittivity (ε_r) profiles.

4.2 Shallow-Layer VIC Distribution

The shallow-layer VIC was calculated by integrating soil-sample measurements with FWI-derived relative permittivity, following the workflow detailed in the Methods section (Fig.

https://doi.org/10.5194/egusphere-2026-828
Preprint. Discussion started: 9 March 2026

10). Due to differences in sampling depths among the four sites, the displayed depth ranges of shallow-layer VIC varied accordingly. Overall, Huashixia exhibited relatively low VIC, consistent with moderate ice accumulation and comparatively high unfrozen water content, whereas Hela, Shuangchagou, and Maduo showed higher VIC, indicative of extensively developed ice-rich frozen soils. Spatially, the shallow-layer VIC maps revealed pronounced heterogeneity, with localized high-ice zones corresponding to discrete ice lenses or ice-rich pockets. Shuangchagou, in particular, exhibited notable small-scale variability, reflecting local anomalies embedded within the generally frozen background. Collectively, these spatial patterns captured the distribution of shallow VIC at each site and provided a critical near-surface reference for constructing the fitted permittivity-resistivity-ice relationships and for analyzing deeper VIC distribution.

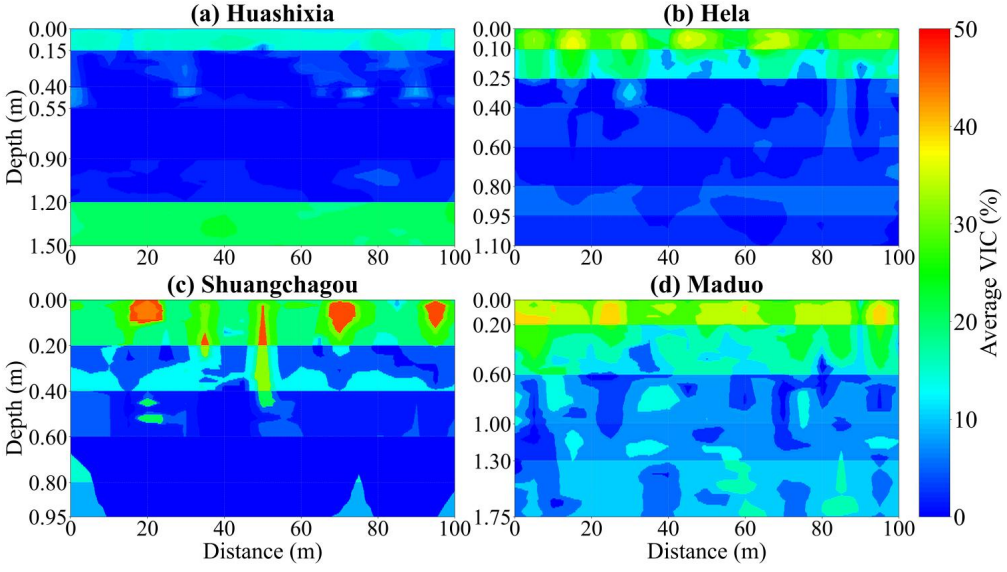

Fig. 10. Shallow-layer VIC profiles.

4.3 Deep-Layer VIC Estimation

Because direct sampling of deep subsurface layers was challenging, quantifying the spatial distribution of VIC below the sampling depth required an indirect approach. In this study, deep-layer VIC was estimated by extrapolating the relationships between VIC and electromagnetic parameters established in the shallow subsurface, where both direct measurements and electromagnetic observations were available. Apparent resistivity and relative

https://doi.org/10.5194/egusphere-2026-828
Preprint. Discussion started: 9 March 2026

permittivity provided complementary characterizations of the same subsurface materials. Because VIC, unfrozen VWC, and pore structure jointly controlled both apparent resistivity and relative permittivity, the empirical relationships derived in the shallow layer could be reasonably extended to deeper intervals where only electromagnetic data were available. Shallow VIC (y, %) was jointly fitted with apparent resistivity (ρ, Ω·m) and FWI-derived relative permittivity (ε_r) to construct predictive surfaces. Among seven tested two-parameter models (linear, quadratic, cubic, exponential, power-law, logarithmic, and hyperbolic), the two-parameter cubic model consistently demonstrated the best performance across all four sites, indicating a pronounced nonlinear coupling between VIC and electromagnetic parameters. The mathematical expressions of the optimal fitting functions for each site were summarized in Table 2.

Table 2 Fitted surface equations.

Field site	Fitted surface
Huashixia	y=31.5 - 0.007 ρ - 5.6 ε_r + 0.000004 ρ^2 + 0.002 ρ ε_r + 0.4 ε_r^2 - 0.0000000008 ρ^3 - 0.0000007 ρ^2 ε_r - 0.0002 ρ ε_r^2 - 0.01 ε_r^3
Hela	y=54.0 + 0.002 ρ - 3.4 ε_r - 0.0000007 ρ^2 - 0.0002 ρ ε_r + 0.1 ε_r^2 + 0.00000000007 ρ^3 + 0.00000003 ρ^2 ε_r + 0.000005 ρ ε_r^2 - 0.002 ε_r^3
Shuangchagou	y=56.2 + 0.0002 ρ - 3.6 ε_r - 0.0000001 ρ^2 + 0.000002 ρ ε_r + 0.1 ε_r^2 + 0.00000000002 ρ^3 - 0.000000004 ρ^2 ε_r - 0.0000004 ρ ε_r^2 - 0.002 ε_r^3
Maduo	y=51.5 - 0.002 ρ - 4.3 ε_r + 0.0000005 ρ^2 + 0.0003 ρ ε_r + 0.2 ε_r^2 - 0.00000000005 ρ^3 - 0.00000006 ρ^2 ε_r - 0.00001 ρ ε_r^2 - 0.004 ε_r^3

Based on the optimal cubic fitting surfaces, the 20 m deep VIC distribution was estimated (Fig. 11). Across the entire depth range, Huashixia exhibited generally low VIC, consistent with the moderate VIC inferred from its electromagnetic characteristics. In contrast, Hela, Shuangchagou, and Maduo displayed markedly higher VIC, featuring laterally continuous ice-rich zones and locally enhanced ice accumulation, indicative of the widespread development of thick ice-bearing permafrost. Shuangchagou, in particular, showed pronounced lateral variability, with localized high-VIC anomalies embedded within a moderately ice-rich background, highlighting the strong heterogeneity of the deep permafrost strata. These VIC distributions were spatially consistent with the previously derived apparent resistivity sections

https://doi.org/10.5194/egusphere-2026-828
Preprint. Discussion started: 9 March 2026

and relative permittivity profiles obtained from FWI, further validating the reliability and physical plausibility of VIC estimation based on integrated electromagnetic observations.

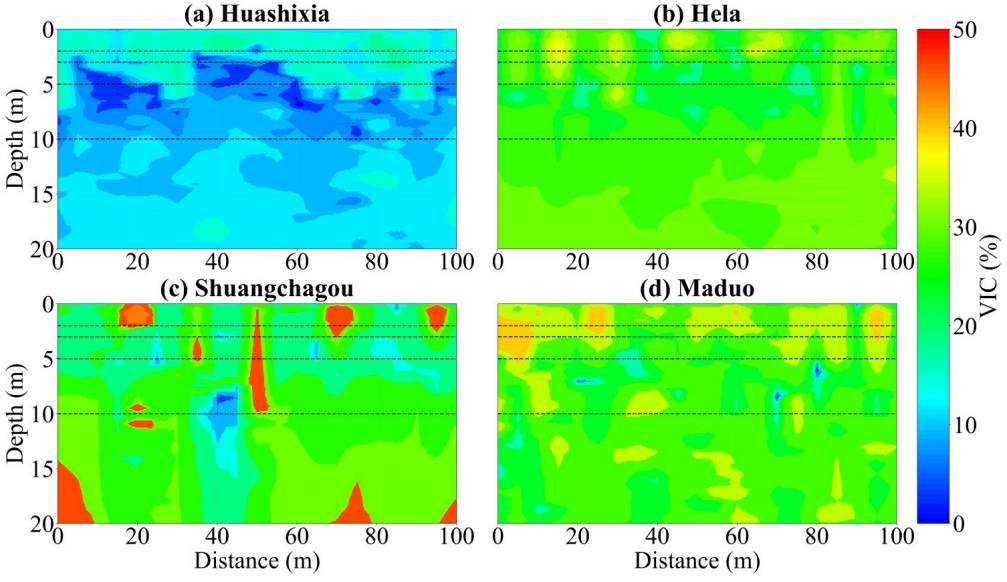

Fig. 11. Deep-layer VIC profiles.

4.4 Validation of VIC Estimates

To evaluate the consistency of the predicted VIC with previous studies, depth-dependent VIC obtained in this study was compared with reference data reported by Zou et al. (2024) using boxplots (Fig. 12). Overall, the predicted VIC at all four sites exhibited comparable ranges and similar depth-dependent trends relative to the reference values, indicating that the proposed inversion framework effectively captured the primary characteristics of VIC distribution.

It should be noted that the predicted VIC was generally slightly lower than the reference values, particularly at greater depths. This systematic discrepancy could be reasonably explained by two main factors. First, the reference study did not explicitly account for unfrozen water, which may have led to overestimation when TVWC is directly interpreted as VIC. In contrast, the present study separated liquid water from ice by integrating FWI-derived relative permittivity, yielding a physically constrained estimate of VIC. Second, the field measurements in this study were more recent, and ongoing regional warming may have caused partial thawing of permafrost

https://doi.org/10.5194/egusphere-2026-828
Preprint. Discussion started: 9 March 2026

in the upper layers, resulting in lower VIC compared to earlier observations. Despite these differences, the predicted VIC values fell within the range of previously reported values, and the mean values showed good agreement with literature data, particularly for Hela and Maduo. This suggested that, after accounting for methodological and temporal differences, the electromagnetic parameter-based inversion approach provided a robust representation of VIC distribution and was consistent with independent estimations.

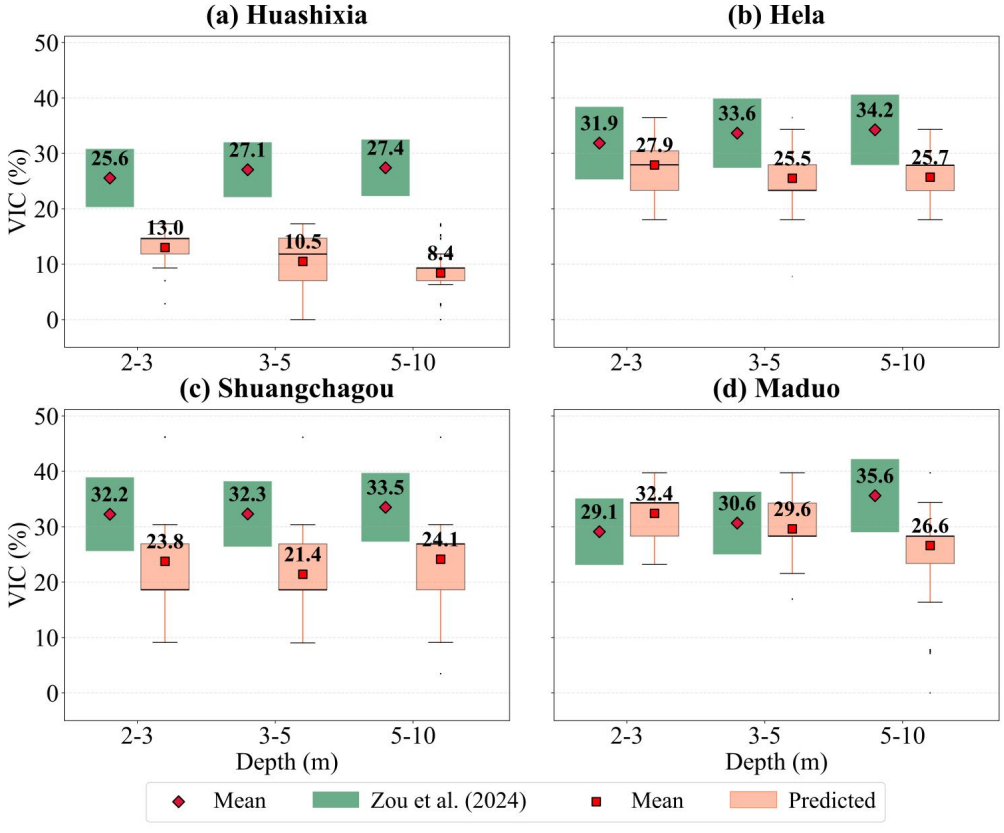

Fig. 12. Comparison of boxplots with those reported by Zou et al. (2024).

The quantitative performance of the proposed approach was further evaluated using root RMSE and MAE metrics for different depth intervals, as summarized in Table 3. Overall, the error metrics confirmed a good agreement between the predicted and reference VIC, while also revealing site-specific and depth-dependent variations in estimation accuracy. Huashixia exhibited relatively larger errors across all depths, with RMSE and MAE increasing with depth. This was attributed to moderate VIC and higher moisture variability, which reduced the

https://doi.org/10.5194/egusphere-2026-828
Preprint. Discussion started: 9 March 2026

sensitivity of electromagnetic parameters to VIC. Shuangchagou showed intermediate error levels, reflecting pronounced lateral heterogeneity, where localized ice-rich anomalies embedded in moderately frozen backgrounds increased the uncertainty of VIC estimates. In contrast, Hela and Maduo consistently displayed lower RMSE and MAE values across all depth intervals. Both sites featured thick and laterally continuous ice-rich permafrost, which enhanced the stability of the empirical relationships between electromagnetic parameters and VIC. Consequently, the predicted VIC at these sites aligned closely with reference data, particularly in shallow and intermediate depth ranges.

Table 3 RMSE and MAE for VIC estimates.

	RMSE(%)				MAE(%)			
Site / Depth	Huashixia	Hela	Shuangchagou	Maduo	Huashixia	Hela	Shuangchagou	Maduo
2-3m	12.9	5.7	11.3	5.6	12.6	4.5	10.2	4.7
3-5m	17.1	9.1	12.9	4.9	16.5	8.2	12.1	4.1
5-10m	19.2	9.1	11.6	10.1	19.0	8.5	10.4	9.0
Total	16.6	8.1	11.9	7.2	16.0	7.1	10.9	6.0

5. Discussion

5.1 Sensitivity Analysis of Electromagnetic Parameters

To evaluate the sensitivity of radar signals to VIC, simulations were first performed under uniform ice distribution using 100 MHz and 400 MHz, which matched the dual-frequency radar system used in the field (Fig. 13). As VIC increased, relative permittivity decreased and wavelength increased, reflecting enhanced ice-related dielectric contrast. Signal amplitude showed a frequency-dependent response. At 100 MHz, amplitude remained high at low VIC and varied nonlinearly at higher VIC. At 400 MHz, amplitude decreased steadily with increasing VIC and showed stronger attenuation. These results indicated that 100 MHz radar was more sensitive to bulk VIC, while 400 MHz radar was more affected by attenuation and had limited sensitivity to deeper ice layers.

https://doi.org/10.5194/egusphere-2026-828
Preprint. Discussion started: 9 March 2026

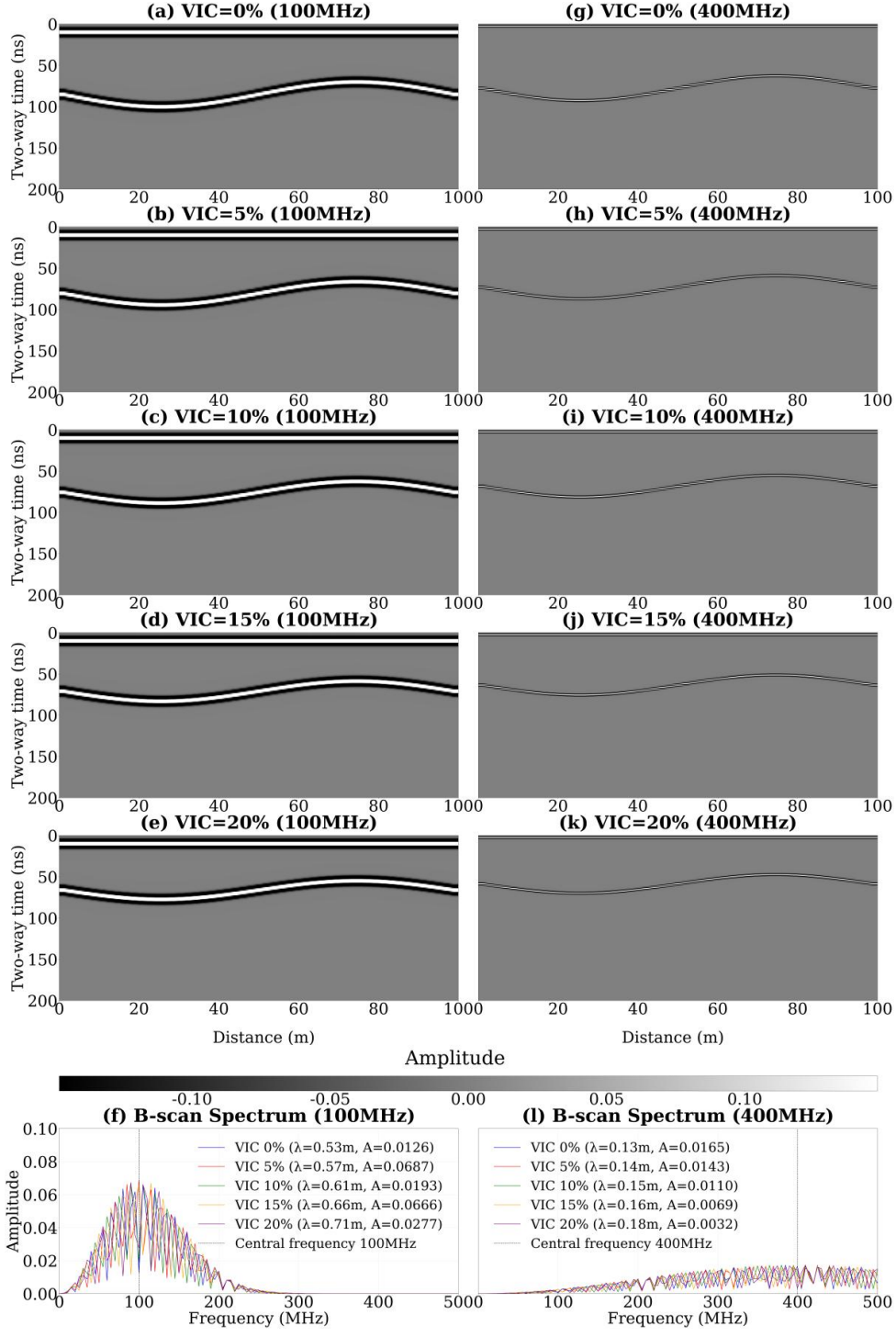

Fig. 13. Radar responses and spectral plots at different frequencies under uniform ice distribution.

https://doi.org/10.5194/egusphere-2026-828
Preprint. Discussion started: 9 March 2026

Radar responses were further simulated under random ice distribution to represent heterogeneous frozen ground conditions (Fig. 14). At 100 MHz, increasing VIC enhanced scattering, resulting in diffuse reflections and irregular amplitude variations caused by randomly distributed ice interfaces. Although signal coherence was reduced, low-frequency radar still exhibited strong penetration capability and could effectively detect subsurface ice layers down to depths of approximately 20 m. At 400 MHz, signal attenuation increased rapidly with VIC and accumulated with depth, leading to progressively weaker and less coherent reflections in deeper layers, together with a sharp reduction in effective penetration depth. These results indicated that low-frequency radar was better suited for detecting bulk VIC and deeper subsurface structures at depths of approximately 20 m, whereas high-frequency radar was primarily effective for resolving fine-scale ice structures in the shallow subsurface, at depths of around 5 m.

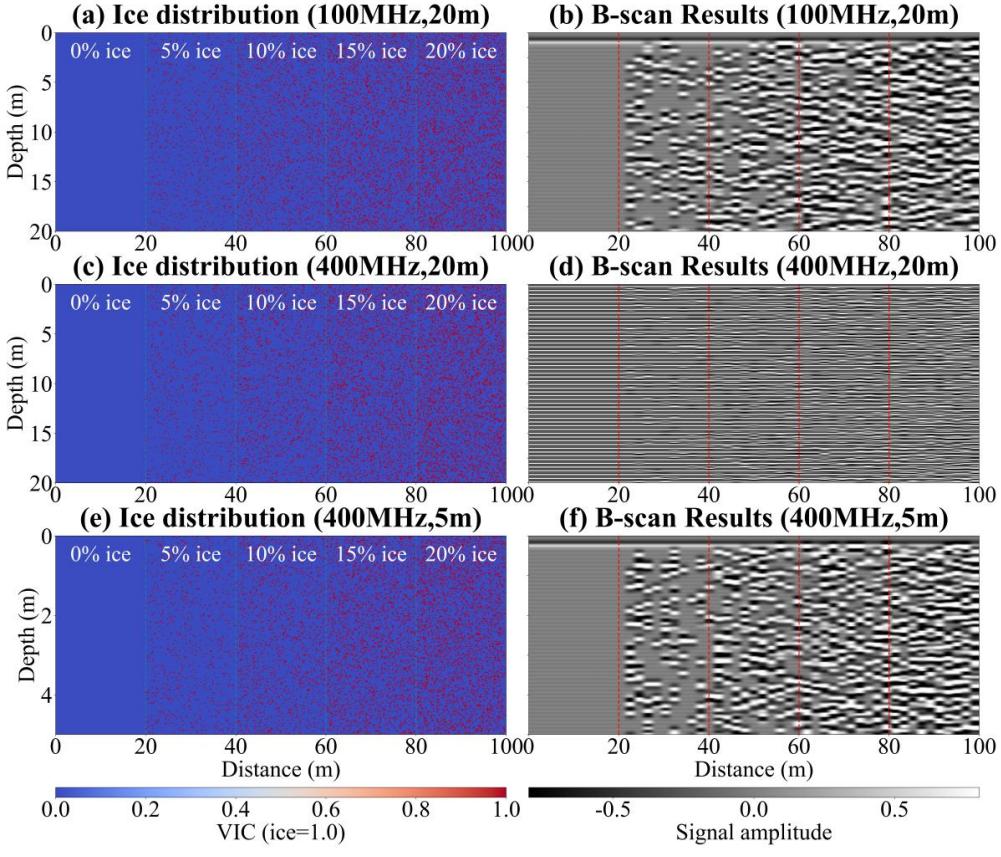

Fig. 14. Radar responses at different frequencies and depths under random ice distribution.

https://doi.org/10.5194/egusphere-2026-828
Preprint. Discussion started: 9 March 2026

The stability of the VIC inversion framework was evaluated by perturbing relative permittivity (ε_r±5%) and apparent resistivity (ρ±10%) (Table 4). The estimated VIC was highly sensitive to changes in relative permittivity but showed negligible response to apparent resistivity perturbations. Increasing relative permittivity led to lower VIC estimates, while decreasing relative permittivity produced higher VIC. This behavior reflected the three-phase composition of frozen soil, in which ice replaces unfrozen water and reduces the relative permittivity (Guo et al., 2018). Since radar wave velocity, wavelength, and reflection strength were directly controlled by relative permittivity, small perturbations produced clear changes in inversion results. In contrast, apparent resistivity variations had little effect because radar wave propagation at 100 MHz was dominated by dielectric polarization rather than conductive loss.

Table 4 Sensitivity analysis of VIC estimation with ε_r and ρ (Ω·m).

	Depth(m)	pred	ε_r-5%	ε_r+5%	ρ-10%	ρ+10%	Zou et al. (2024)
Huashixia	2-3	13.0	13.6	12.4	13.0	13.0	[20.3%, 30.8%]
	3-5	10.5	11.2	9.9	10.5	10.5	[22.1%, 32.0%]
	5-10	8.4	9.1	7.7	8.4	8.4	[22.3%, 32.5%]
Hela	2-3	27.9	28.9	27.0	27.9	27.9	[25.3%, 38.4%]
	3-5	25.5	26.5	24.5	25.5	25.5	[27.4%, 39.9%]
	5-10	25.7	26.7	24.8	25.7	25.7	[27.9%, 40.6%]
Shuangchagou	2-3	23.6	24.6	22.6	23.6	23.6	[25.6%, 38.9%]
	3-5	21.3	22.4	20.2	21.3	21.3	[26.4%, 38.2%]
	5-10	24.1	25.1	23.1	24.1	24.1	[27.3%, 39.7%]
Maduo	2-3	32.4	33.1	31.7	32.4	32.4	[23.1%, 35.1%]
	3-5	29.6	30.4	28.9	29.6	29.6	[25.0%, 36.3%]
	5-10	26.6	27.5	25.8	26.6	26.6	[29.0%, 42.2%]

5.2 Similarity Analysis of Forward Modeling

A similarity analysis was conducted to assess the agreement between measured and modeled GPR profiles and the reliability of the forward modeling framework. Huashixia was presented as an example (Fig. 15), with results from other sites presented in Fig. S1-S3. Measured data were

https://doi.org/10.5194/egusphere-2026-828
Preprint. Discussion started: 9 March 2026

lightly processed and modeled profiles were enhanced to match spatial and depth sampling; both were smoothed and normalized before comparison. Comprehensive similarity values across all sites ranged from 0.56 to 0.72, indicating good agreement.

The comparison showed that the forward models reproduced the main reflectors and the overall signal pattern of the measured profiles. Differences were mainly limited to localized details, while the dominant structural features related to VIC distribution were well captured. Analyses of different profile segments confirmed that the core reflection characteristics remained consistent across the entire survey line. Quantitative similarity metrics further supported these measurements. High values of local sign consistency and trend correlation indicated strong agreement in reflection polarity and signal variation. Lower local structural similarity reflected limitations in reproducing fine-scale random scattering, which did not affect the representation of large-scale ice structures. These results demonstrated that the forward models provided a reliable structural representation of subsurface ice conditions.

Together with the sensitivity analysis, the similarity results confirmed that the proposed modeling and inversion framework was physically consistent and stable. The framework effectively linked electromagnetic responses to VIC and provided a reliable basis for VIC estimation in permafrost regions, particularly where direct subsurface observations were limited.

https://doi.org/10.5194/egusphere-2026-828
Preprint. Discussion started: 9 March 2026

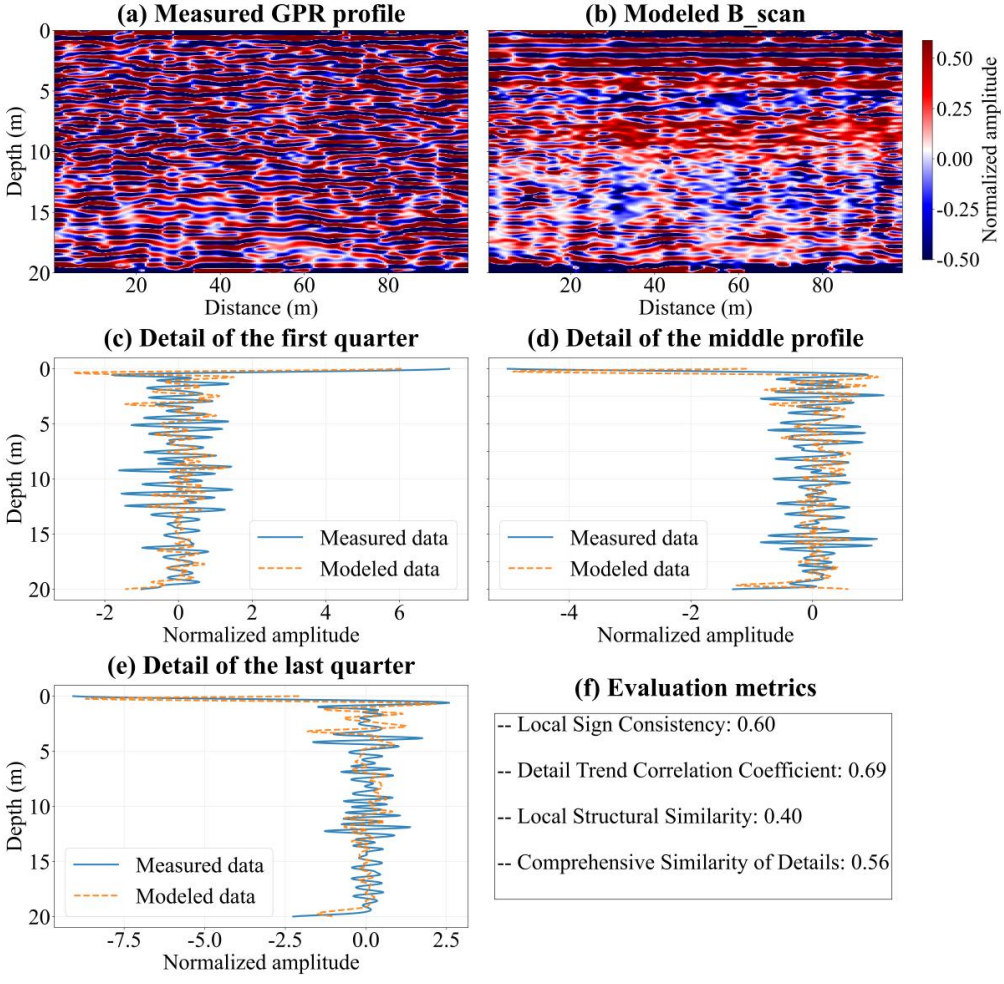

Fig. 15. Comparison of measured and modeled radar profiles for Huashixia.

5.3 Advantages and Uncertainty of Joint Inversion

The joint inversion used OCTEM data to build a forward model of the subsurface and GPR measurements to refine it. OCTEM provided depth-resolved apparent resistivity and helped define dielectric and conductive properties. The forward model was then compared with measured GPR data. Differences between the modeled and measured radar responses were used to adjust the model. This approach ensured that the final model matched both OCTEM-based apparent resistivity structure and GPR-observed waveforms, producing reliable VIC estimates.

https://doi.org/10.5194/egusphere-2026-828
Preprint. Discussion started: 9 March 2026

This method reduced uncertainty because OCTEM constrained large-scale structure and depth while GPR refined shallow layers and fine-scale features. The two data sources complemented each other, making the model less sensitive to noise or anomalies within individual datasets. It performed well even in complex permafrost with heterogeneous ice and soil properties, although some uncertainty remained. The relationship between relative permittivity, apparent resistivity, and VIC was complex, and local variations in soil or ice could still introduce errors. Using both datasets reduced these errors, but further optimization was needed to improve accuracy in highly heterogeneous ground.

6. Conclusion

This study integrated GPR and OCTEM observations to develop a physically constrained framework for quantitative estimation of VIC in high-altitude permafrost regions. The main conclusions are summarized as follows.

(1) Distinct permafrost and ground-ice characteristics were observed across the four study sites. Huashixia was characterized by relatively low apparent resistivity and moderate ice accumulation, whereas Hela exhibited comparatively stable permafrost conditions. Shuangchagou showed pronounced local anomalies, where discrete ice lenses were embedded within a frozen background. In contrast, Maduo was dominated by ice-rich permafrost with thick ice-bearing layers. These site-specific differences highlighted the strong spatial heterogeneity of permafrost structure and provided a geophysical basis for quantitative ground-ice assessment.

(2) By jointly fitting shallow-layer VIC with apparent resistivity and relative permittivity, a dual-parameter cubic response surface model was established. This model outperformed alternative formulations, demonstrating a strong nonlinear coupling between electromagnetic properties and VIC. Sensitivity analysis further indicated that VIC estimates were more sensitive to variations in relative permittivity than to apparent resistivity, underscoring the dominant role of radar-derived parameters in shallow ice quantification.

(3) Estimated VIC at depths of 2-10 m showed that Huashixia had relatively low average VIC, approximately 8-15%, whereas Hela, Shuangchagou, and Maduo generally exceeded 20%.

https://doi.org/10.5194/egusphere-2026-828
Preprint. Discussion started: 9 March 2026

These spatial patterns were consistent with apparent resistivity distributions and forward-modeled electromagnetic structures. Comparison with previous studies indicated good agreement in both ice-content magnitude and vertical variation trends. Error assessment yielded total root mean square errors of 16.6%, 8.1%, 11.9%, and 7.2% for Huashixia, Hela, Shuangchagou, and Maduo, respectively, with lower errors predominantly associated with sites characterized by thick and laterally continuous ice-rich permafrost.

Data availability

Data will be made available on request.

Author Contributions

Wei Chen: Methodology, Formal analysis, Visualization, Writing—original draft. Min Xu: Conceptualization, Methodology, Resources, Formal analysis, Investigation, Supervision, Writing—review and editing. Weibin Luo: Investigation, Supervision, Writing—review and editing. Haidong Han: Investigation, Supervision, Writing—review and editing. Wu Wang: Investigation, Supervision, Writing—review and editing. Xi Zhang: Investigation, Supervision, Writing—review and editing. Xingdong Li: Supervision, Writing—review and editing.

Competing interests

The authors declare that they have no conflict of interest.

Acknowledgements

Thanks to the National Tibetan Plateau Data Center (TPDC) for providing ground te mperature data for 2013–2015 (https://data.tpdc.ac.cn/en/data/a7807b90-5e38-4450-836a-0f1f2af77ab3).

https://doi.org/10.5194/egusphere-2026-828
Preprint. Discussion started: 9 March 2026

Financial support

This research was supported by a project of the Strategic Priority Research Program (Category B) of the Chinese Academy of Sciences (Grant No. XDB0950103).

References

Aga, J., Boike, J., Langer, M., Ingeman-Nielsen, T., Westermann, S., 2023. Simulating ice segregation and thaw consolidation in permafrost environments with the CryoGrid community model. The Cryosphere 17, 4179–4206. https://doi.org/10.5194/tc-17-4179-2023

Anbazhagan, P., Bittelli, M., Pallepati, R.R., Mahajan, P., 2020. Comparison of soil water content estimation equations using ground penetrating radar. Journal of Hydrology 588, 125039. https://doi.org/10.1016/j.jhydrol.2020.125039

Brandt, O., Langley, K., Kohler, J., Hamran, S.-E., 2007. Detection of buried ice and sediment layers in permafrost using multi-frequency Ground Penetrating Radar: A case examination on Svalbard. Remote Sensing of Environment 111, 212–227. https://doi.org/10.1016/j.rse.2007.03.025

Briggs, M.A., Campbell, S., Nolan, J., Walvoord, M.A., Ntarlagiannis, D., Day-Lewis, F.D., Lane, J.W., 2017. Surface Geophysical Methods for Characterising Frozen Ground in Transitional Permafrost Landscapes: Surface Geophysical Methods for Characterising Frozen Ground. Permafrost and Periglac. Process. 28, 52–65. https://doi.org/10.1002/ppp.1893

Busch, S., Van Der Kruk, J., Bikowski, J., Vereecken, H., 2012. Quantitative conductivity and permittivity estimation using full-waveform inversion of on-ground GPR data. Geophysics 77, H79–H91. https://doi.org/10.1190/geo2012-0045.1

Chen, Y., Li, S., Wang, L., Mittermeier, M., Bernier, M., Ludwig, R., 2024. Retrieving freeze-thaw states using deep learning with remote sensing data in permafrost landscapes. International Journal of Applied Earth Observation and Geoinformation 126, 103616. https://doi.org/10.1016/j.jag.2023.103616

D18 Committee, n.d. Test Methods for Laboratory Determination of Water (Moisture) Content of Soil and Rock by Mass. https://doi.org/10.1520/D2216-19

Du, E., Wang, L., Zhao, L., Zhou, H., Liu, S., Zou, D., Liu, G., Xiao, Y., Hu, G., Li, Z., Gao, J., Wang, C., Wang, Y., Wang, X., Chen, W., 2025. Quantifying the soil water content of the permafrost active layer using InSAR deformation. Journal of Hydrology 661, 133660. https://doi.org/10.1016/j.jhydrol.2025.133660

Du, E., Zhao, L., Zou, D., Li, R., Wang, Z., Wu, X., Hu, G., Zhao, Y., Liu, G., Sun, Z., 2020. Soil Moisture Calibration Equations for Active Layer GPR Detection—a Case Study Specially for the Qinghai–Tibet Plateau Permafrost Regions. Remote Sensing 12, 605. https://doi.org/10.3390/rs12040605

Ekimova, V., Nelson, M.A., Sullivan, T., Douglas, T.A., Epstein, H.E., Jull, M.G., 2026. Characterizing near-surface permafrost in Utqiaġvik, Alaska, using Electrical Resistivity Tomography and Ground Penetrating Radar. The Cryosphere 20, 265–283. https://doi.org/10.5194/tc-20-265-2026

Faucher, B., LeBlanc, A.-M., Oldenborger, G., Carrière, E., Lacelle, D., Letellier, Philippe, 2024. Ground ice content of the frozen active layer and near-surface permafrost in the Rankin Inlet area, Nunavut, Canada.

https://doi.org/10.5194/egusphere-2026-828
Preprint. Discussion started: 9 March 2026

International Permafrost Association (IPA). https://doi.org/10.52381/ICOP2024.80.1

García-Pereira, F., González-Rouco, J.F., Meabe-Yanguas, N., De Vrese, P., Steinert, N.J., Jungclaus, J., Lorenz, S., 2025. Permafrost sensitivity to soil hydro-thermodynamics in historical and scenario simulations with the MPI-ESM. The Cryosphere 19, 5959–5981. https://doi.org/10.5194/tc-19-5959-2025

Garcıa, S.G., Bretones, A.R., Olmedo, B.G., Martın, R.G., n.d. Finite difference time domain methods.

Ge, J., Sun, H., Liu, R., Huang, Z., Tian, B., Liu, L., Zheng, Z., 2025. Permafrost thawing characterization in engineering scale by multi-geophysical methods: A case study from the Tibet Plateau. Engineering Geology 350, 108012. https://doi.org/10.1016/j.enggeo.2025.108012

Gerhards, H., Wollschläger, U., Yu, Q., Schiwek, P., Pan, X., Roth, K., 2008. Continuous and simultaneous measurement of reflector depth and average soil-water content with multichannel ground-penetrating radar. Geophysics 73, J15–J23. https://doi.org/10.1190/1.2943669

Guo, Y., Xu, S., Shan, W., 2018. Development of a frozen soil dielectric constant model and determination of dielectric constant variation during the soil freezing process. Cold Regions Science and Technology 151, 28–33. https://doi.org/10.1016/j.coldregions.2018.03.006

Harris, R.H., Evans, S.G., Marshall, S.T., Godsey, S.E., Parsekian, A.D., 2025. Using Ground-Penetrating Radar to Infer Ice Wedge Characteristics Proximal to Water Tracks. JGR Earth Surface 130, e2024JF007832. https://doi.org/10.1029/2024JF007832

Hilbich, C., Hauck, C., Mollaret, C., Wainstein, P., Arenson, L.U., 2022b. Towards accurate quantification of ice content in permafrost of the Central Andes – Part 1: Geophysics-based estimates from three different regions. The Cryosphere 16, 1845–1872. https://doi.org/10.5194/tc-16-1845-2022

Hodson, T.O., 2022. Root-mean-square error (RMSE) or mean absolute error (MAE): when to use them or not. Geosci. Model Dev. 15, 5481–5487. https://doi.org/10.5194/gmd-15-5481-2022

Hu, G., Sun, Z., Zhao, L., Chen, D., Zou, D., Ping, C.-L., Zhang, W., Xiao, Y., Liu, G., Li, R., Wu, X., Wu, Y., Cheng, G., 2025. The crucial role of ground ice in slowing permafrost degradation. Science Bulletin S2095927325011715. https://doi.org/10.1016/j.scib.2025.11.042

Jin, H., Huang, Y., Bense, V.F., Ma, Q., Marchenko, S.S., Shepelev, V.V., Hu, Y., Liang, S., Spektor, V.V., Jin, X., Li, Xinyu, Li, Xiaoying, 2022. Permafrost Degradation and Its Hydrogeological Impacts. Water 14, 372. https://doi.org/10.3390/w14030372

Jin, X., Jin, H., Luo, D., Sheng, Y., Wu, Q., Wu, J., Wang, W., Huang, S., Li, X., Liang, S., Wang, Q., He, R., Serban, R.D., Ma, Q., Gao, S., Li, Y., 2022. Impacts of Permafrost Degradation on Hydrology and Vegetation in the Source Area of the Yellow River on Northeastern Qinghai-Tibet Plateau, Southwest China. Front. Earth Sci. 10, 845824. https://doi.org/10.3389/feart.2022.845824

Lacelle, D., Fisher, D.A., Verret, M., Pollard, W., 2022. Improved prediction of the vertical distribution of ground ice in Arctic-Antarctic permafrost sediments. Commun Earth Environ 3, 31. https://doi.org/10.1038/s43247-022-00367-z

Li, C., Zhao, L., Wang, L., Liu, S., Zhou, H., Li, Z., Liu, G., Du, E., Zou, D., Hou, Y., 2023. Ground Deformation and Permafrost Degradation in the Source Region of the Yellow River, in the Northeast of the Qinghai-Tibet Plateau. Remote Sensing 15, 3153. https://doi.org/10.3390/rs15123153

Li, J., Sheng, Y., Wu, J., Feng, Z., Ning, Z., Hu, X., Zhang, X., 2016. Landform-related permafrost characteristics in the source area of the Yellow River, eastern Qinghai-Tibet Plateau. Geomorphology 269, 104–111. https://doi.org/10.1016/j.geomorph.2016.06.024

Li R., Wu Q., Li X., Sheng Y., Hu G., Cheng G., Zhao L., Jin H., Zou D., Wu X., 2019. Characteristic, changes and impacts of permafrost on Qinghai-Tibet Plateau. Chin. Sci. Bull. 64, 2783–2795. https://doi.org/10.1360/TB-2019-0191

https://doi.org/10.5194/egusphere-2026-828
Preprint. Discussion started: 9 March 2026

Lin, Z., Gao, Z., Fan, X., Niu, F., Luo, J., Yin, G., Liu, M., 2020. Factors controlling near surface ground-ice characteristics in a region of warm permafrost, Beiluhe Basin, Qinghai-Tibet Plateau. Geoderma 376, 114540. https://doi.org/10.1016/j.geoderma.2020.114540

Liu, G., Zhao, L., Xie, C., Zou, D., Wu, T., Du, E., Wang, L., Sheng, Y., Zhao, Y., Xiao, Y., Wang, C., Wang, Y., 2022. The Zonation of Mountain Frozen Ground under Aspect Adjustment Revealed by Ground-Penetrating Radar Survey—A Case Study of a Small Catchment in the Upper Reaches of the Yellow River, Northeastern Qinghai–Tibet Plateau. Remote Sensing 14, 2450. https://doi.org/10.3390/rs14102450

Liu, H., Dai, D., Zou, L., He, Q., Meng, X., Chen, J., 2024. Refined Modeling of Heterogeneous Medium for Ground-Penetrating Radar Simulation. Remote Sensing 16, 3010. https://doi.org/10.3390/rs16163010

Liu, L., Song, C., He, L., Wang, S., Feng, X., Liu, C., 2025. Fast ground penetrating radar dual-parameter full waveform inversion method accelerated by hybrid compilation of CUDA kernel function and PyTorch. https://doi.org/10.48550/arXiv.2506.20513

Liu, S., Zhao, L., Wang, L., Liu, L., Zou, D., Hu, G., Sun, Z., Zhang, Y., Chen, W., Wang, X., Wang, M., Zhou, H., Qiao, Y., 2025. Ground surface deformation in permafrost region on the Qinghai-Tibet Plateau: A review. Earth-Science Reviews 265, 105109. https://doi.org/10.1016/j.earscirev.2025.105109

Mollaret, C., Wagner, F.M., Hilbich, C., Scapozza, C., Hauck, C., 2020. Petrophysical Joint Inversion Applied to Alpine Permafrost Field Sites to Image Subsurface Ice, Water, Air, and Rock Contents. Front. Earth Sci. 8, 85. https://doi.org/10.3389/feart.2020.00085

Niu, F., Jiao, C., Luo, J., He, J., He, P., 2023. Three-Dimensional Numerical Modeling of Ground Ice Ablation in a Retrogressive Thaw Slump and Its Hydrological Ecosystem Response on the Qinghai-Tibet Plateau, China. Int J Disaster Risk Sci 14, 566–585. https://doi.org/10.1007/s13753-023-00503-z

Roustaei, M., Pumple, J., Harvey, J., Froese, D., 2025. Ground ice estimation in permafrost samples using industrial computed tomography and multi-sensor core logging and comparison to destructive measurements. The Cryosphere 19, 4259–4275. https://doi.org/10.5194/tc-19-4259-2025

Stoyanovich, G.M., Pupatenko, V.V., Sukhobok, Y.A., 2015. Detection of ground ice using ground penetrating radar method. Sciences in Cold and Arid Regions.

Teixeira, F.L., Sarris, C., Zhang, Y., Na, D.-Y., Berenger, J.-P., Su, Y., Okoniewski, M., Chew, W.C., Backman, V., Simpson, J.J., 2023. Finite-difference time-domain methods. Nat Rev Methods Primers 3, 75. https://doi.org/10.1038/s43586-023-00257-4

Tomaškovičová, S., Ingeman-Nielsen, T., 2024. Coupled thermo–geophysical inversion for permafrost monitoring. The Cryosphere 18, 321–340. https://doi.org/10.5194/tc-18-321-2024

Wang, L., Dai, Y., Liu, W., Zhou, S., Long, X., Xi, Z., Xue, J., Wang, W., 2024. Deep learning transient electromagnetic inversion for seawater intrusion. Journal of Geophysics and Engineering 21, 1810–1821. https://doi.org/10.1093/jge/gxae107

Wang, S., Sheng, Y., Li, J., Wu, J., Cao, W., Ma, S., 2018. An Estimation of Ground Ice Volumes in Permafrost Layers in Northeastern Qinghai-Tibet Plateau, China. Chin. Geogr. Sci. 28, 61–73. https://doi.org/10.1007/s11769-018-0932-z

Wang, W., Wu, T., Zhao, L., Li, R., Xie, C., Qiao, Y., Zhang, H., Zhu, X., Yang, S., Qin, Y., Hao, J., 2018. Hydrochemical characteristics of ground ice in permafrost regions of the Qinghai-Tibet Plateau. Science of The Total Environment 626, 366–376. https://doi.org/10.1016/j.scitotenv.2018.01.097

Warren, C., Giannopoulos, A., Giannakis, I., 2016. gprMax: Open source software to simulate electromagnetic wave propagation for Ground Penetrating Radar. Computer Physics Communications 209, 163–170. https://doi.org/10.1016/j.cpc.2016.08.020

https://doi.org/10.5194/egusphere-2026-828
Preprint. Discussion started: 9 March 2026

Wei, H., Shi Z.L., Wang B.,Liu M., 2023. The applicability research of opposing coils transient electromagnetics method in Pb-Zn orn exploration. [in Chinese]. Journal of Yunnan University: Natural Sciences Edition 45, 1-8.

Wu, Y., Nakagawa, S., Kneafsey, T.J., Dafflon, B., Hubbard, S., 2017. Electrical and seismic response of saline permafrost soil during freeze - Thaw transition. Journal of Applied Geophysics 146, 16–26. https://doi.org/10.1016/j.jappgeo.2017.08.008

Xiao, Y., Liu, G., Hu, G., Zou, D., Li, R., Du, E., Wu, T., Wu, X., Zhao, G., Zhao, Y., Zhao, L., 2025. Mapping Mountain Permafrost via GPR-Augmented Machine Learning in the Northeastern Qinghai–Tibet Plateau. Remote Sensing 17, 2015. https://doi.org/10.3390/rs17122015

Yang, G., Xie, C., Wu, T., Wu, X., Zhang, Y., Wang, W., Liu, G., 2022. Detection of permafrost in shallow bedrock areas with the opposing coils transient electromagnetic method. Front. Environ. Sci. 10, 909848. https://doi.org/10.3389/fenvs.2022.909848

Yang, Y., Guo, X., Wu, Q., Jin, H., Liu, F., 2023b. Formation processes of shallow ground ice in permafrost in the Northeastern Qinghai-Tibet Plateau: A stable isotope perspective. Science of The Total Environment 863, 160967. https://doi.org/10.1016/j.scitotenv.2022.160967

Yang, Y., Wu, Q., Guo, X., Zhou, L., Yao, H., Zhang, D., Zhang, Z., Chen, J., Liu, G., 2024. First comprehensive stable isotope dataset of diverse water units in a permafrost-dominated catchment on the Qinghai–Tibet Plateau. Earth Syst. Sci. Data 16, 3755–3770. https://doi.org/10.5194/essd-16-3755-2024

Yang, Y., Wu, Q., Jiang, G., Zhang, P., 2020. Ground ice at depths in the Tianshuihai Lake basin on the western Qinghai-Tibet Plateau: An indication of permafrost evolution. Science of The Total Environment 729, 138966. https://doi.org/10.1016/j.scitotenv.2020.138966

You, Y., Yang, M., Yu, Q., Pan, X., Guo, L., Wang, X., Wu, Q., 2018. Factors influencing the reliability of grounded and floating ice distinguishing based on ground penetrating radar reflection amplitude. Cold Regions Science and Technology 154, 1–8. https://doi.org/10.1016/j.coldregions.2018.06.008

Yuan, L., Zhao, L., Li, R., Hu, G., Du, E., Qiao, Y., Ma, L., 2020. Spatiotemporal characteristics of hydrothermal processes of the active layer on the central and northern Qinghai–Tibet plateau. Science of The Total Environment 712, 136392. https://doi.org/10.1016/j.scitotenv.2019.136392

Zhang, M., Feng, X., Bano, M., Xing, H., Wang, T., Liang, W., Zhou, H., Dong, Z., An, Y., Zhang, Y., 2022. Review of Ground Penetrating Radar Applications for Water Dynamics Studies in Unsaturated Zone. Remote Sensing 14, 5993. https://doi.org/10.3390/rs14235993

Zhang, Z., Wang, Q., Jin, Q., Wang, M., n.d. Exploring Ground Ice Dynamics in Central Qinghai–Tibet Plateau Permafrost Region Using SAR Interferometry, Landsat, and ICESat-2 Data.

Zhao, H., Sun, H., Zhang, Y., Liu, R., Chen, L., Liu, S., 2025. Assessing goaf in steep coal seam over complex topography using semi-airborne transient electromagnetic method: a case study in Xinjiang China. Bull Eng Geol Environ 84, 342. https://doi.org/10.1007/s10064-025-04342-8

Zou, D., Pang, Q., Zhao, L., Wang, L., Hu, G., Du, E., Liu, G., Liu, S., Liu, Y., 2024. Estimation of Permafrost Ground Ice to 10 m Depth on the Qinghai-Tibet Plateau. Permafrost & Periglacial 35, 423–434. https://doi.org/10.1002/ppp.2226

Zwieback, S., Iwahana, G., Chang, Q., Meyer, F., 2025. InSAR estimates of excess ground ice concentrations near the permafrost table. ISPRS Journal of Photogrammetry and Remote Sensing 223, 261–273. https://doi.org/10.1016/j.isprsjprs.2025.03.004